A Platinum Open Access Journal for Organic Chemistry

Paper

Free to Authors and Readers

DOAJ Sea

Arkivoc **2027** (2) 202612641

Characterization of tioconazole mesylate. Single crystal X-ray diffraction, Hirshfeld surface analysis, stability and DFT-assisted infrared spectral assignment

Aldana B. Moroni,[a,b,§] María Florencia Silveira,[a] and Natalia L. Calvo[a,b,*]

[a]Instituto de Química Rosario "Dr. Edmundo A. Rúveda" (IQUIR, CONICET-UNR), Suipacha 531, Rosario S2002LRK, Argentina; [b]Área de Análisis de Medicamentos, Facultad de Ciencias Bioquímicas y Farmacéuticas, Universidad Nacional de Rosario, Suipacha 531, Rosario S2002LRK, Argentina; [§]Present address: Instituto de Investigaciones en Ingeniería Ambiental, Química y Biotecnología Aplicada (INGEBIO), Av. Pellegrini 3314, Rosario S2002QEO, Argentina

[*]Email: calvo@iquir-conicet.gov.ar

Dedicated with gratitude to Professor Teodoro S. Kaufman from his students and co-workers

Received 06-28-2026 **Accepted** 08-31-2026 **Published on line** 09-15-2026

Abstract

Tioconazole mesylate (TCZ-Ms) is an anhydrous and stable solid form, more soluble than tioconazole. New contributions to its analytical profile are provided, including its characterization by single crystal X-ray diffractometry and Hirshfeld surface analysis, heat-stability monitoring, nuclear magnetic resonance spectra and an improved, more rational assignment of its mid-infrared spectrum based on theoretical calculations.

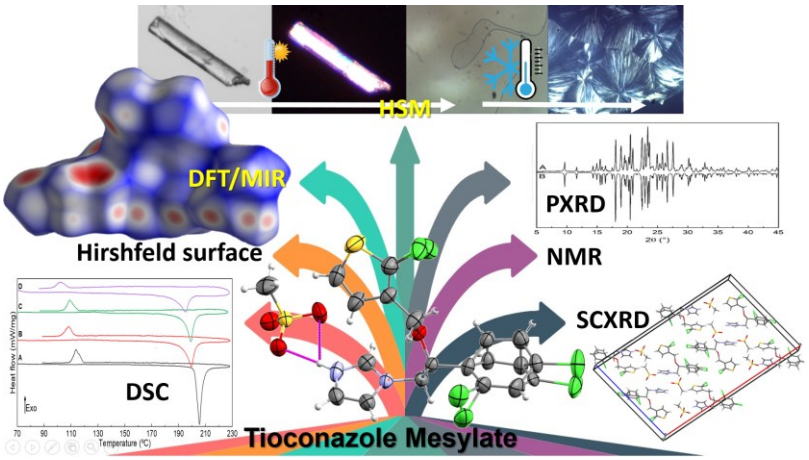

Keywords: Tioconazole mesylate, solid-state characterization, single crystal X-ray diffraction, Hirshfeld surface

 ©AUTHOR(S)

Introduction

Tioconazole (TCZ, Figure 1) is 1-(2-[(2-chloro-thien-3-yl)methoxy]-2-[2,4-dichlorophenyl]ethyl)-1*H*-imidazole, a widely employed antifungal agent, which belongs to the family of the azoles. Its antifungal activity is ascribed to the interaction between the nitrogen atom of the imidazole ring to the iron atom of the heme moiety in the binding site of the enzyme 14-α-demethylase, which causes depletion of ergosterol.[1] The drug is a white to almost white weakly basic (pK_a 6.51-6.61) imidazole derivative,[2] characterized by a low melting point (80 °C).[3] It is highly lipophilic, with log P (partition octanol:water) 4.23-4.86,[4,5] and displays poor aqueous solubility (16.5 mg L^{-1}),[6] which is further reduced at pH 6.8 (phosphate buffer), to reach 1.7 mg L^{-1}.[7] Despite having a stereogenic center and slightly different metabolism between enantiomers, it is marketed as a racemate.[8]

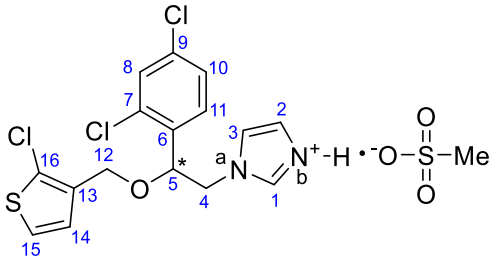

Figure 1. Chemical structure and atom numbering of TCZ-Ms. The asterisk (*) indicates the stereogenic center.

TCZ is primarily classified in the Biopharmaceutical Classification System (BCS) as a Class II drug (high permeability and low aqueous solubility). Its markedly hydrophobic nature hinders its dissolution, bioavailability, and antifungal activity, requiring engineered formulations to overcome these limitations. However, since TCZ is an ionizable molecule, the formation of salts is an acceptable option to improve its hydrophilicity and aqueous solubility. This endeavor, which benefits additionally from the availability of a series of selectable suitable counter ions, seems attractive in view that the current solid-state landscape of the drug remains unexpectedly simple and largely unexplored.

In fact, the drug has no known polymorphs and a simple search in the Cambridge Structural Database (https://www.ccdc.cam.ac.uk/ structures/?) with the keyword "Tioconazole" revealed only 22 hits, of which two belong to TCZ itself.[9] Perlovich *et al.* have recently prepared the anhydrous (1:1) salts with malonic (SAPBAQ) and fumaric (SAPBEU) acids, along with a DL-tartrate monohydrate (1:1:1, SAPBIY).[7] In addition, other known related substances are the 1:1 salts with acids like hydrobromic (YOBSER), 2-chloro-4-nitrobenzoic (YOBSIV), nicotinic (YOBTES), and sulfuric (as the bisulfate, YOBTUI), and cocrystals with terephthalic (YOBVAQ, YOBVAQ01), L-tartaric (YOBTAO), and oxalic acids (YOBTIW).[10] Besides, we have recently disclosed the anhydrous (1:1) salts with maleic, *p*-toluenesulfonic (YOBTOC) and methanesulfonic acids.[11]

Furthermore, salt hydrates have been obtained, such as the bis(tioconazole) sulfate heptahydrate (2:1:7, YOBWEV),[10] along with the pentahydrate (2:1:5, YOBVOE), the oxalate tetrahydrate (2:1:4, YOBVUK), the fumarate monohydrate (1:1:1, YOBSOB) and hemihydrate (2:2:1, YOBSUH), and the L-tartrate hydrate (1:1:3.4, YOBWAR).[10] In addition, we have recently prepared and characterized the hydrochloride hemihydrate (ZIYCET, ZIYCET01) and described the hydrochloride hydrate (1:1:0.1, ZIYCIX).[6]

Within the current drug development paradigm, the analytical profile of an active pharmaceutical ingredient (API) serves to fully characterize it from a chemical, physical, and microbiological perspective, in

 ©AUTHOR(S)

order to guarantee its quality, safety, and efficacy, in such a way that it can be regarded as its scientific "identity fingerprint". Our recent exploration of the solid state of various APIs[12,13] led us to investigate the solid-state landscape of TCZ through the preparation and characterization of relevant salt derivatives. As part of this effort, we have prepared and partially characterized tioconazole mesylate (TCZ-Ms), finding that its solubility, intrinsic dissolution rate, and dissolution profile are greatly improved compared to TCZ, to the point of representing those of a BCS Class I drug (high permeability and high aqueous solubility) for a 0.1 mg cm^{-2} min^{-1} low/high solubility cut-off.[14] However, we were unable to find suitable conditions to prepare single crystals of the phase for diffractometry, its thermal stability was incompletely characterized, and its mid-infrared spectrum was assigned just by comparison with similar salts.

Mesylates are attractive counterions because they do not form hydrates and usually provide stable and non-volatile salts that do not disproportionate and can be better handled during formulation than their parent bases, especially when they are low melting point solids with poor flow properties and subject to plastic deformation, as is the case of TCZ. Another key aspect is the disproportionation of salt forms, which is less common in sulfonate salts as the byproducts of the resulting reaction are stable and non-volatile. Hence, TCZ-Ms may hold good prospects for future development.[15]

Therefore, herein we report additional critical aspects on the characterization of TCZ-Ms, including its single crystal diffraction characteristics, along with the corresponding Hirshfeld surface analysis. Furthermore, we also provide new insights on the thermal stability of the salt, details of its solution nuclear magnetic resonance (NMR) spectra, and a more rigorous density functional theory (DFT)-based assignment of the main bands found in its mid-infrared spectrum.

Results and Discussion

Preparation of the solid phase and single crystals

The TCZ-Ms phase was obtained as a white solid (mp 200-202 °C) by precipitation in diethyl ether (Et_2O), after reaction of equimolar amounts of TCZ and methanesulfonic acid (MsOH). This was followed by a solvent screening stage, in order to find the best solvent for crystallization. Among the different tested solvents, Et_2O and methanol proved to be unsuitable, whereas acetone and acetonitrile afforded very thin needles (attached to one another) and small needles, respectively. However, chloroform furnished long single crystals, which were considered suitable for single crystal X-ray diffractometry (SCXRD).

Nuclear magnetic resonance

Characterization of the solid phase through mono- (1D) and and bi-dimensional (2D) NMR spectroscopy (Figures S1-S6) served to demonstrate the 1:1 stoichiometry of the salt and provided evidence that the solid phase is anhydrous. Characteristic signals of the mesylate counterion (Ms^-, $MeSO_3^-$) were found at δ_H 2.33 (s, 3H, *Me*SO_3^-) and δ_C 36.4 ppm (*Me*SO_3^-). Evidence of a protonated nitrogen was observed at δ_H 4.03 (bs, 1H, N^+-*H*).

The unequivocal assignment of the signals and comparison with those of TCZ revealed a strong shielding of C2 ($\Delta\delta$ -8.5 ppm) and smaller effects on the remaining carbon atoms associated with the imidazole ring, C1, C3, and C4 (Table S2), suggesting that N_b is the protonation site.[18] The latter was further confirmed by the ^{15}N Heteronuclear Multiple Bond Correlation (HMBC) experiment, which revealed a single signal for both nitrogen atoms at δ_N -203.5 ppm, involving chemical shift variations ($\Delta\delta_N$) amounting to +8.5 and -84.8 ppm for the proximal (N_a) and distal (N_b) nitrogen atoms, respectively.

 ©AUTHOR(S)

Single-crystal X-ray diffraction

Slow recrystallization of the precipitated salt from $CHCl_3$ afforded single crystals of TCZ-Ms, suitable for SCXRD measurements.

Table 1. Crystallographic and structural refinement data of TCZ-Ms

Variable	*Result*		*Variable*	*Result*
Empirical formula	$C_{16}H_{14}Cl_3N_2OS^+ \cdot CH_3O_3S^-$		F(000)	1984
Molecular weight	483.79		Crystal size (mm^3)	0.338 x 0.096 x 0.061
Crystallographic system	Monoclinic		Data collection range θ (°)	2.201 to 24.442
Space group, Z	C2/*c*, 8		Number of collected reflections	42798
Temperature (K)	298(2)		Number of independent reflections	3412 [R(int) 0.0818]
Unit cell dimensions	a 37.864(4)	α 90	Refinement method	Full matrix least squares in F^2
a, b, c (Å)	b 6.0155(6)	β 102.146(9)	Data / constraints / parameters	3412 / 0 / 309
α, β, γ (°)	c 18.7413(19)	γ 90	Goodness of fit in F^2	1.102
Cell volume ($Å^3$)	4173.2(7)		Final R-indices [I > 2 sigma(I)]	R_1 0.0565, wR_2 0.1103
Calculated density (g/cm^3)	1.540		R-indices (complete data)	R_1 0.0797, wR_2 0.1203
Absorption coefficient (mm^{-1})	0.666		CCDC deposit number	2552715

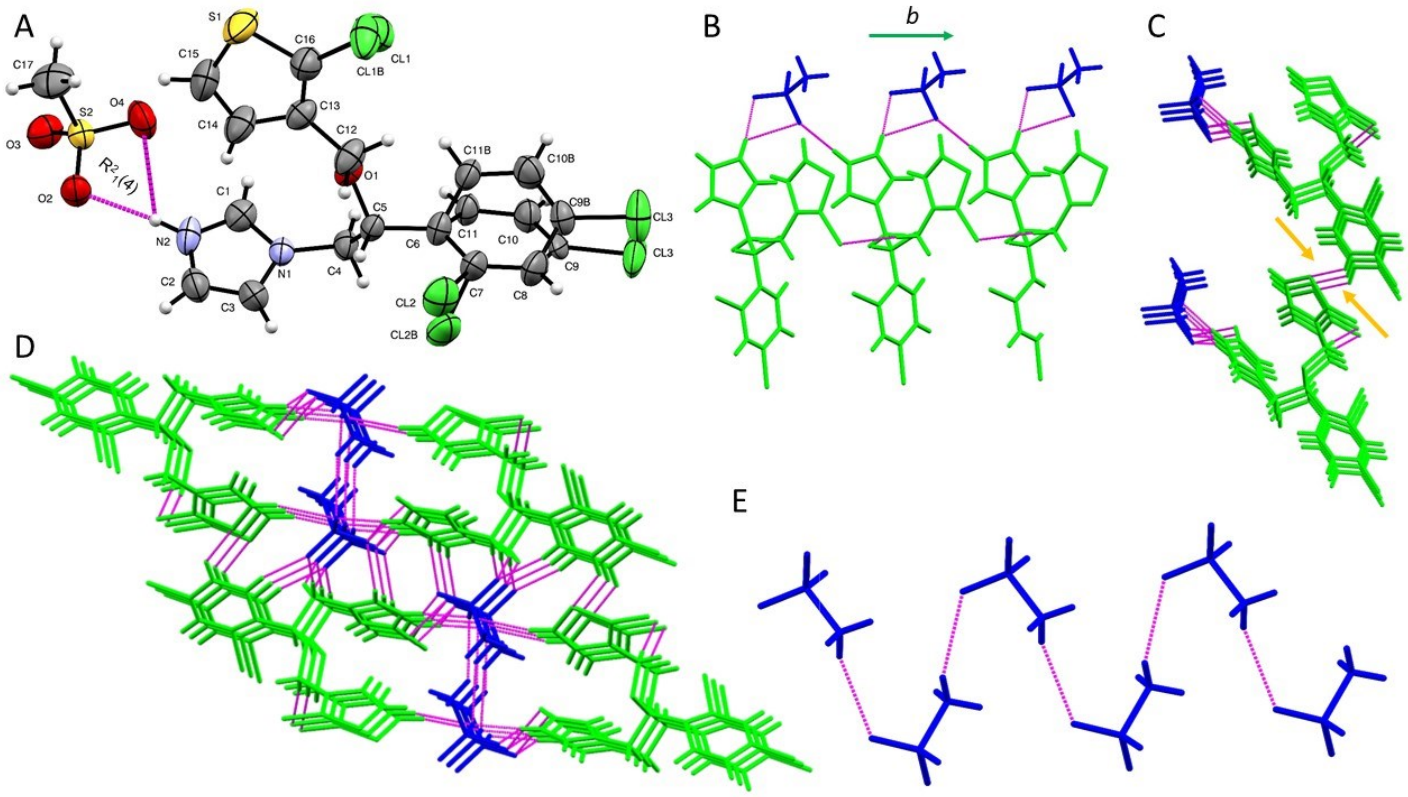

Figure 2. (A) Oak Ridge Thermal Ellipsoid Plot (ORTEP) representation of TCZ-Ms with its atomic labeling (displacement ellipsoids are drawn with a 50% probability level). (B) 1D chains of $TCZH^+$-Ms^--$TCZH^+$-Ms^- units propagated along the *b*-axis. Color by symmetry equivalence. The $TCZH^+$ disorder was omitted for clarity. (C) Interchain interactions (arrows) through $TCZH^+$ units. (D) Chain interactions through counterions. (E) Chain of Ms^- anions. In all graphs, the hydrogen bonds are shown with magenta lines.

 ©AUTHOR(S)

The crystal structure was solved and refined in the monoclinic space group C2/c; key crystallographic parameters, data collection conditions, and refinement details at 298 K are summarized in Table 1. Figure 2 shows the molecular diagram of the salt with the corresponding atomic labeling and aspects of the H-bonding network that stabilizes the crystal. Further details of bond distances and angles, as well as torsion angles and hydrogen bonds are provided as supplementary material. The phase turned out to be anhydrous with a crystallographically independent $TCZH^{+}\cdot Ms^{-}$ ion pair at the asymmetric unit (ASU), with the following lattice parameters: a 37.864(4) Å, b 6.0155(6) Å, c 18.7413(19) Å and β 102.146(9)°. It is observed that in the ASU, the counterions are associated by charge-assisted bifurcated hydrogen bond interactions (N^{+}–H···O^{-}), involving the protonated N of the imidazole ring of the cation and two O of the anion [$N2^{+}$–H2N···$O2^{-}$ (x, y, z) and $N2^{+}$–H2N···$O4^{-}$ (x, y, z)] forming a $R^{2}_{1(4)}$ synthon (Figure 2A). It is worth noting that the $TCZH^{+}$ cation is disordered on three carbons of the phenyl ring (C9-C11) and on the three chlorine atoms (Cl1-Cl3), exhibiting two positions on each of these atoms, with similar occupancy.

The internal C1-N2-C2 angle of the imidazole ring was 110.1(3)°, which is similar to that observed for TCZ-Cl·½H_2O,[6] indicating protonation of the distal N atom and the formation of a salt. The salt structure is consolidated by a three-dimensional network of hydrogen bonds between anions and cations, as well as by interactions between them.

Regarding anion-cation interactions, each methanesulfonate (mesylate, Ms^{-}) anion acts as a hydrogen bond acceptor for five neighboring $TCZH^{+}$ units. The $N2^{+}$–H2N···$O2^{-}$ (x, y, z) and $N2^{+}$–H2N···$O4^{-}$ (x, y, z) interactions, along with the C2–H2···$O4^{-}$ (x, y-1, z) hydrogen bond, form an intercalated chain of $TCZH^{+}$-Ms^{-}-$TCZH^{+}$-Ms^{-} that propagates along the *b*-axis (Figure 2B), where the $TCZH^{+}$ molecules are further connected by C12–H12B···Cl1 (x, y-1, z) bonds. Inter-chain interactions (Figure 2C) occur at the level of the $TCZH^{+}$ units via C10–H10···S1 (x, -y+2, z+1/2) or through multiple instances between counterions in different chains (Figure 2D).

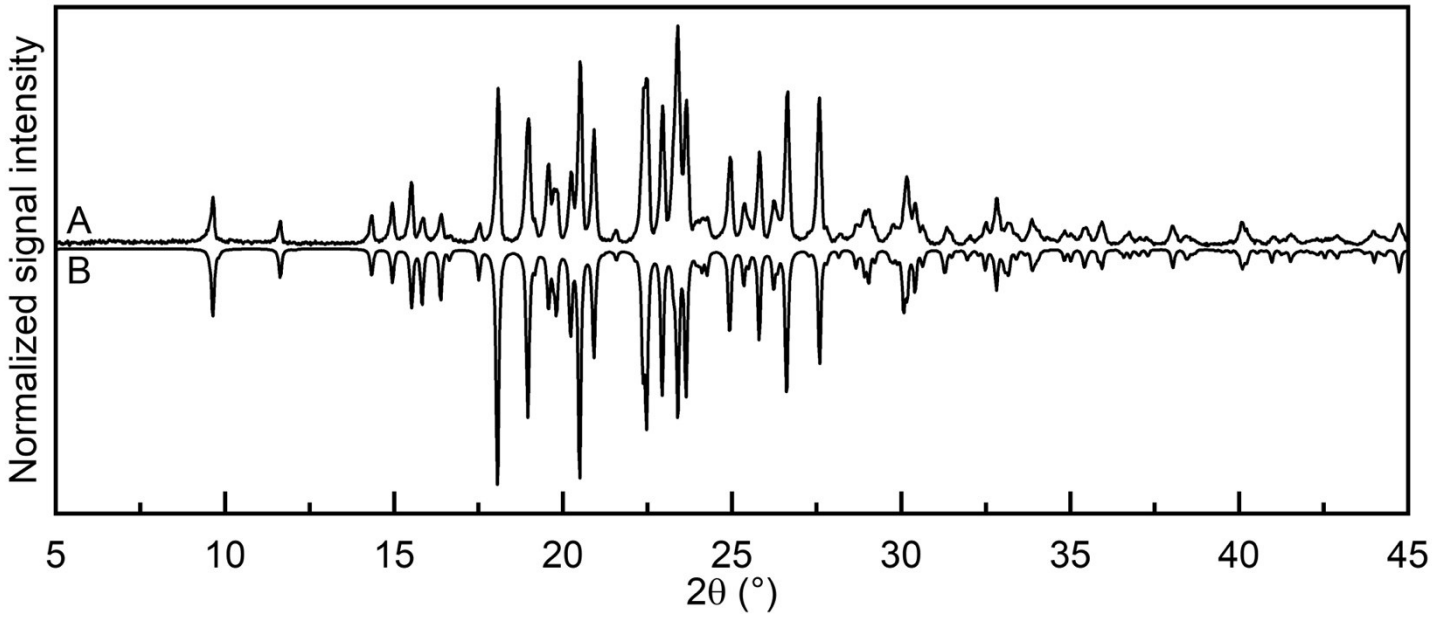

Figure 3. Comparison between the experimental diffractogram of TCZ-Ms (A) with its theoretical counterpart (B), obtained from the single crystal X-ray diffractogram of the solid phase, in the range 2θ 5-45°.

 ©AUTHOR(S)

Three interactions between Ms^- and a third $TCZH^+$ unit are observed via C4−H4A···O3 (-x+3/2, -y+3/2, -z+1), C1−H1···O4 (-x+3/2, -y+3/2, -z+1), and C11−H11···O3 (-x+3/2, -y+3/2, -z+1). There is also an interaction with a fourth unit of the same chain via C4−H4B···O3 (-x+3/2, -y+1/2, -z+1) and with a fifth $TCZH^+$ unit via C15−H15···O2 (-x+3/2, y+1/2, -z+1/2). The anions form hydrogen bonds of the type C17—H17B···O2 (-x+3/2, y+1/2, -z+1/2) with each other, acting as both acceptors and donors, thus producing a zig-zag chain of mesylates (Figure 2E). Therefore, each Ms^- moiety is joined by hydrogen bonds to 5 $TCZH^+$ units, corresponding to three different chains, and to a couple of neighboring Ms^- units. This demonstrates the important acceptor and donor character of this anion, which is capable of transmitting a great three-dimensional cohesion to the structure. A comparison was performed between the experimental diffractogram of TCZ-Ms (Figure 3A), which displayed sharp and well-defined signals free of peaks from its precursors, and the theoretical diffractogram of the salt (Figure 3B), calculated from single crystal data. Full agreement in the position of the peaks was observed, confirming that the microcrystalline powder and the crystals obtained by its recrystallization correspond to the same solid phase.

Hirshfeld surface analysis

Hirshfeld surface analysis and fingerprint plots are a valuable approach for examining intermolecular interactions within a crystal structure, employing its crystallographic information file as input; they provide detailed information on the molecular packing and the contributions of the various interactions to the crystal lattice. Since each crystal structure produces a unique outcome, a three-dimensional Hirshfeld surface with a normalized contact distance (d_{norm}) plot was prepared and two-dimensional fingerprint plots were concomitantly generated. The value of d_{norm} depends on the van der Waals radii (vdWr) of the involved nuclei as well as the values of di and de, which are the distance to the nearest nucleus inside the surface and to the nearest atoms outside the surface, respectively. Both distances are useful to pinpoint the zones where critical interactions take place.[16]

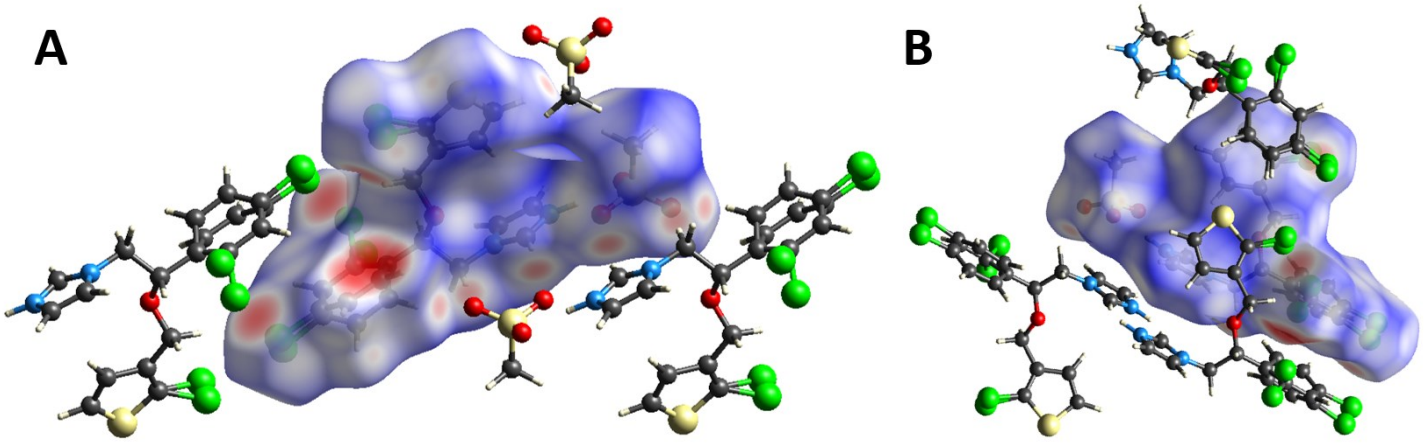

Figure 4. View of the three-dimensional Hirshfeld surface of the asymmetric unit plotted over d_{norm} surrounded by neighboring molecules in a ball and stick presentation. A) H···O/O···H and Cl···Cl interactions; B) H···Cl/Cl···H and Cl···Cl interactions.

An analysis of the intermolecular contacts was then performed in order to assess the presence of hydrogen bonds and other non-covalent interactions within the crystal structure (Figures 4A and 4B) and unveil the most important contributions made by the different intermolecular interactions in TCZ-Ms to its

 ©AUTHOR(S)

crystal packing. The Hirshfeld surface was colored white where the contact distance was the sum of the vdW radii, blue where it was longer (> Σ vdWr), and red where it was shorter (< Σ vdWr), and plotted over the range -0.5592 (red) to +1.0909 (blue) a.u., confirming the presence of a number of non-covalent interactions.

The two red spots in the lower left of the surface of Figure 4.A correspond to Cl···Cl interactions between Cl2-Cl3B, forming a dimer between two cations. The red area closer to the center corresponds to a double H···Cl type interaction between H11B and H10B with Cl2B of a neighboring cation (this molecule was omitted for the sake of clarity). Besides, the interactions in the bottom right represent, from left to right, H···O/O···H contacts between cation and anion, via H11···O3 of the phenyl ring, H4A···O3, and H1···O4 of the imidazole moiety in both directions. In addition, the upper right red spot corresponds to an H···O interaction via the H15···O2 hydrogen bond between the imidazole ring and an oxygen atom of the mesylate anion.

Additionally, in Figure 4.B, the lower right spot is another view of the contact of Cl2B with H11B and H10B. The surface also shows the contact of Cl2 with Cl1B (red area in the middle right), whereas the lower left red area displays the O···H type interaction between O3 and H4B. Finally, the upper right point corresponds to Cl1 B with Cl3, another contact between halogens.

The 2D fingerprint plots (Figure 5) revealed that the most relevant contributions to the total intermolecular interactions, observed as a compact core with three spikes, with a more diffuse surrounding (Figure 5A) are almost evenly distributed between the H···H (24.2%), H···O/O···H (20.2%) and H···Cl/Cl···H (18.3%) contributions. The H···H contacts (Figure 5B) appear as a compact region with a single central spike in the middle of the 2D fingerprint plot, while the H···O/O···H contacts (Figure 5C) are observed as an inverted U-shaped figure of scattered dots with two broad bump symmetrical spikes, centered along the diagonal axis, and the Cl···Cl (Figure 5D), which appear as a rather narrow fusiform shape along the diagonal of the fingerprint plot, and the H···Cl/Cl···H (18.3%) appears as a kind of winged horseshoe (Figure 5E).

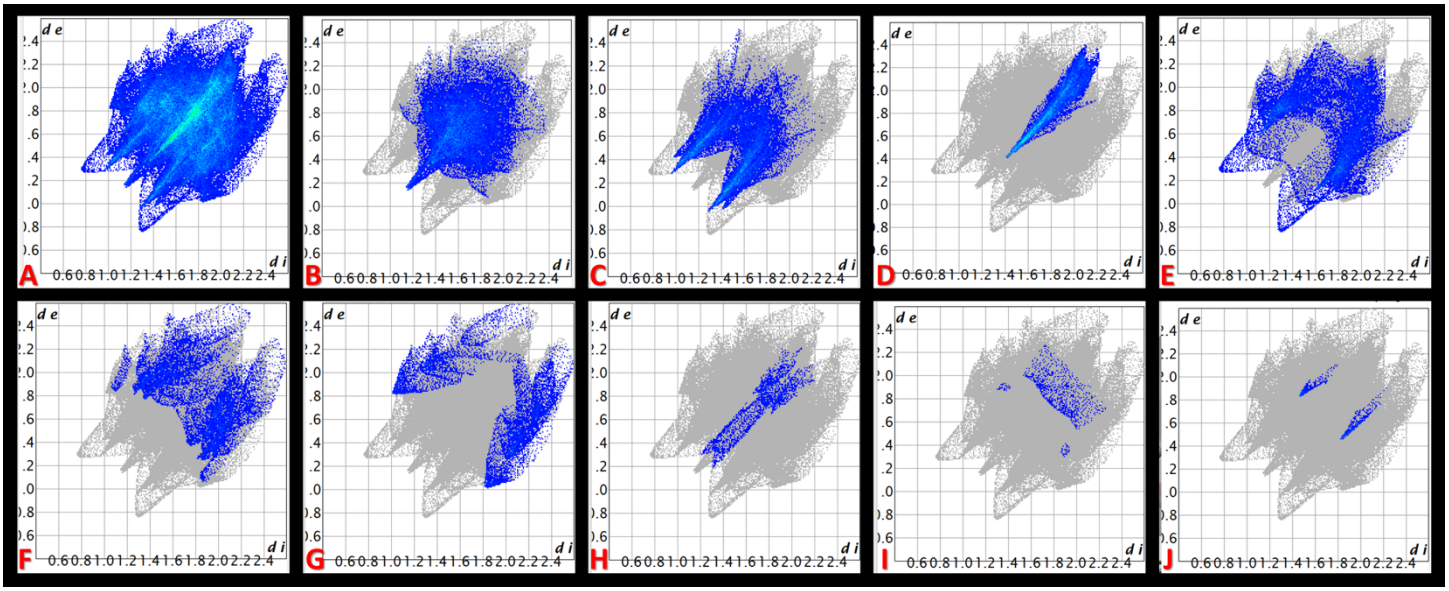

Figure 5. Two-dimensional fingerprint plots for TCZ-Ms showing all interactions (A), along with specific interactions including H···H (B), H···O/O···H (C), Cl···Cl (D), H···Cl/Cl···H (E), H···C/C···H (F), H···S/S···H (G), C···Cl/Cl···C (H), and H···N/N···H (I), and S···O/O···S (J). The di and de values are the closest internal and external distances (in Å) from given points on the Hirshfeld surface, respectively.

 ©AUTHOR(S)

The proportions of these contributions are not fully unexpected, due to the relevant number of oxygen and chlorine atoms present in the molecule, which serves to explain the relative importance of their interactions, and the noteworthy hydrogen content of the salt, which is present in both of its components, and whose interactions suggest that hydrogen bonding should play a major role in the crystal packing.

The contributions to the Hirshfeld surface from other interatomic interactions include H···C/C···H (Figure 5F), which are displayed as a U-shaped graph center at the diagonal axes (10.4%), and the reciprocal H···S/S···H contacts which appear as two symmetrical broad wings and contribute 7% to the Hirshfeld surface (Figure 5G). In comparison, the C···Cl/Cl···C (2.0%) contacts, which appear along the diagonal axis (Figure 5H) and the H···N/N···H contacts (0.8%) shown in Figure 5I along with the S···O/O···S contacts (Figure 5J) represent additional, minor participations.

Mid Infrared (MIR) spectrum

The observed infrared spectrum of TCZ–Ms (Figure S8), which confirmed salification of TCZ, was assigned on the basis of theoretical calculations and compared with the spectrum of TCZ (Table S6).[17] In general, despite the calculations performed on a structure of TCZ-Ms modeled in vacuum, which exhibited some conformational differences with regard to the structure acquired by SCXRD, the vibrational bands of both spectra of TCZ–Ms showed very good agreement, confirming the proposed structure and the presence of the expected functional groups, particularly the imidazole moiety and the Ms^- counterion. The linear regression between the calculated and experimentally observed frequencies yielded a slope of 0.9961 ± 0.0045 and an intercept of −7.4912 ± 6.7821 (Figure S9). Neither parameter differs significantly from the expected values of 1 and 0, respectively, indicating that the fitted line is statistically consistent with the identity line y=x.

The observed bands closely matched most of the calculated (calcd.) frequencies, with typical deviations in the range ~10–20 cm^{-1}, indicating strong consistency between theory and experiment. A perfect agreement was not expected, as differences arise from the limitations of the harmonic approximation employed in the theoretical calculations and the influence of intermolecular interactions (including hydrogen bonding, crystal packing, and other crystal field effects) that usually modify conformational features such as rotations about single bonds. These details are not fully captured by the theoretical model.

The low-wavenumber region (600–800 cm^{-1}) displayed bands at 747, 735, 644, and 623 cm^{-1}, which corresponded well with the calculated values (761, 717, 643, 625 cm^{-1}) for vibrations assigned to out-of-plane C–H bending modes ($\gamma_{C–H}$). They confirmed the substitution pattern of the aromatic rings and the integrity of the ring structure in the salt. Going deeper into the fingerprint region, the bands at 997 and 870 cm^{-1} were in good agreement with calculated absorptions (1012 and 870 cm^{-1}) for the in-plane C–H bending mode ($\delta_{C–H}$) of the aromatic system, while the strong band found at 1047 cm^{-1} was assigned to the $\upsilon_{C–O}$ stretching of the ether group (calcd. 1050 cm^{-1}), further supporting the molecular framework.

The sulfonate group (SO_3^-) was clearly identified by its multiple characteristic absorptions. The bands detected at 932 and 904 cm^{-1} (calcd. 948 and 910 cm^{-1}) were attributed to $\upsilon_{S–O}$ stretching vibrations, whereas the strong bands observed at 1184 and 1032 cm^{-1} (calcd. 1184 and 1026 cm^{-1}) were assigned to the asymmetric and symmetric $\upsilon_{S=O}$ stretching modes, respectively. The agreement in this region was excellent, confirming the presence of the Ms^- anion and its interaction with the tioconazolium cation ($TCZH^+$).

Regarding the latter, the interaction is through the imidazole ring, which has characteristic stretching mode vibrations ($\upsilon_{C=N}$ and $\upsilon_{C–N}$). Their identification is difficult due to the mixing of other vibrations in this region. However, they were also faithfully reproduced by the computations. The band of the $\upsilon_{C–N}$ stretching was found at 1084 cm^{-1} (calcd. 1081 cm^{-1}), while the $\upsilon_{C=N}$ stretching mode (calcd. 1494 cm^{-1}) was assigned to

 ©AUTHOR(S)

the 1472 cm^{-1} band. Interestingly, it has been observed that in TCZ, the υ_{C-N} stretch vibrations are coupled with the $\upsilon_{C=C}$ stretch modes.[17]

Additionally, the band at 1584 cm^{-1} (calcd. 1573 cm^{-1}) was assigned to the δ_{N-H} bending mode of the imidazole ring, suggesting the involvement of one of its nitrogen atoms in protonation or hydrogen bonding. This conjecture was further supported by the presence of a band at 3178 cm^{-1}, which was ascribed to the υ_{N-H} stretching mode of the protonated imidazole moiety, confirming salt formation.

Furthermore, the absorptions at 1559 and 1531 cm^{-1} perfectly matched the corresponding calculated values (1559 and 1531 cm^{-1}) and were attributed to the characteristic aromatic $\upsilon_{C=C}$ stretching vibration. The presence of multiple substituents tends to broaden the bands, which are shifted to lower wavenumbers due to the heavy substituents on the ring. In TCZ, the bands found at 1562 and 1433 cm^{-1} were assigned to the $\upsilon_{C=C}$ of the thiophene ring, whereas signals at 1589, 1562, 1467, 1388, 1281, 1184 and 1137 cm^{-1} were attributed to the phenyl ring. Finally, in the high-frequency region, the bands detected at 3005, 2967 and 2947 cm^{-1} displayed excellent agreement with the corresponding calculated values for alkyl moieties (3012, 2952 and 2946 cm^{-1}) and therefore were assigned to aliphatic υ_{C-H} stretching vibrations. The C–H stretching of methylene and methine groups are at lower frequencies than those of the aromatic C–H ring stretching; however, the latter could be barely detected, as weak bands were expected.

Thermal behavior and stability

The noteworthy stability of the solid phase was inferred from its high temperature at 5% mass loss (T_{d5} 310 °C).[18] Repeated heating and cooling cycles, further confirmed such predictions, observing that the solid withstands these conditions without evident degradation, and displays a crystallization exotherm, which was observed in the ~95-125 °C range (Figure 6).

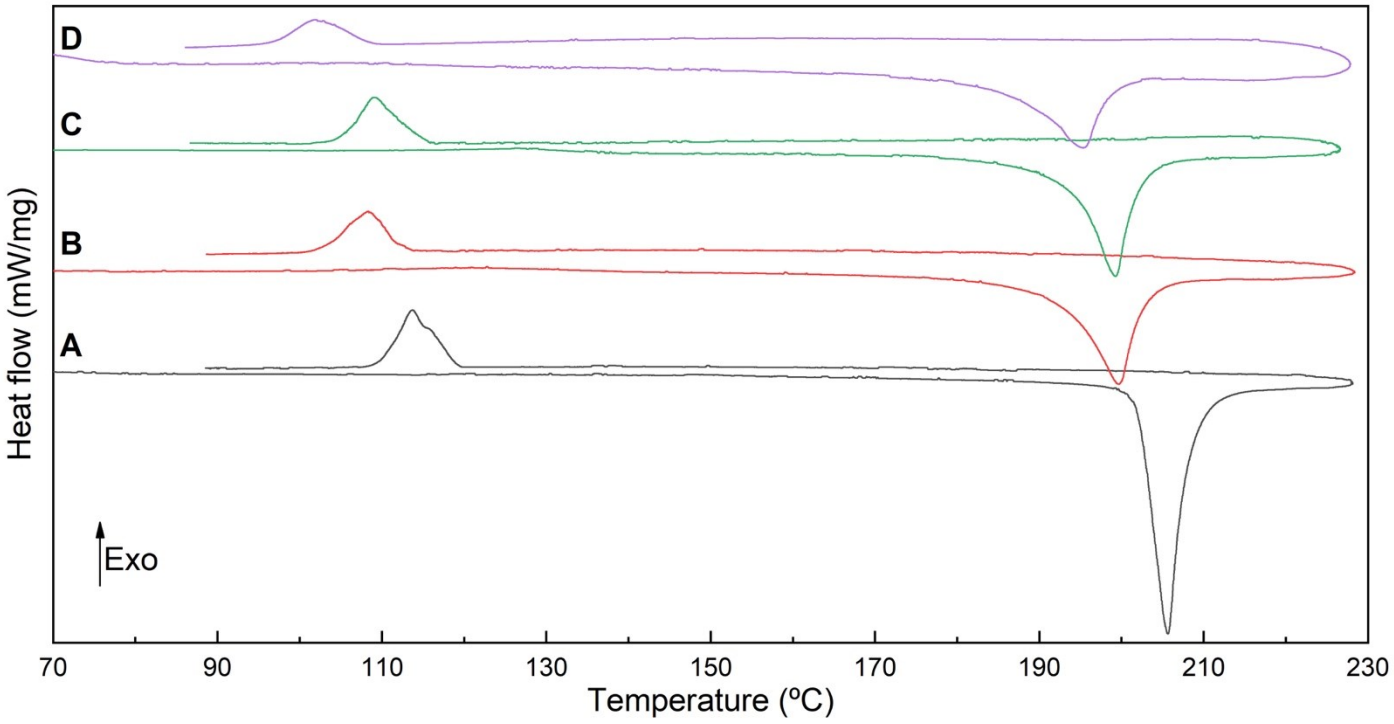

Figure 6. Stability of TCZ-Ms, according to differential scanning calorimetry (DSC) curves after a number of heating and cooling cycles. Cycle N° 1 (A); cycle N° 2 (B); cycle N° 4 (C) and cycle N° 8 (D).

 ©AUTHOR(S)

However, a small drift in the peak of the melting endotherm (T_{max} 205.6 °C in the first cycle to 195.4 °C in the eighth cycle) along with changes in its magnitude were observed. It was conjectured that this may be a result of slight modifications in the particle size of the solid, that take place in the salt upon lattice collapse, and its level of disorder (Table S7). Furthermore, because both ions are small and mobile, the cooling rate may strongly affect crystal packing, with faster cooling resulting in less ordered crystals and broader melting regions.

The variable position of the crystallization exotherm may be attributed to nucleation memory, and melt structural organization effects, since crystallization is nucleation-controlled and highly sensitive to short-range ionic organization. Repeated melting and cooling changes these factors, and even when the sample appears fully melted, slightly above the melting point small residual crystal fragments, ionically associated clusters and short-range ordered domains can still survive. In addition, strong electrostatic interactions between the counterions in the salt may result in persistent ion pairs and small aggregates in the melt. On subsequent cooling, these may act as nucleation templates promoting crystallization. Peak broadening may also point out to some structural disorder. The observed events pointed more to a solid-state reorganization phenomenon than to slow decomposition, and to verify this hypothesis, the solids were examined by thermomicroscopy, MIR spectroscopy and powder X-ray diffractometry (PXRD).

In the thermomicroscopic analysis (Figure 7) it was observed that the crystal (Figure 7A) is birefringent under polarized light (Figure 7D) and that its melting event is in agreement with the endotherm observed in the DSC curve. As expected, upon melting (Figure 7B) the birefringence is lost (Figure 7E); however, it becomes somehow restored (Figure 7F) after solidification of the melted species (Figure 7C). The recrystallization event was detected in a range approximately coincident with the exotherm observed in the DSC curves. Their presence in the DSC traces is not in a fixed place, because they respond to the sudden release of excess energy of the system, which undergoes concomitant solidification. As a result of the whole process, the initial and final solids display different shapes.

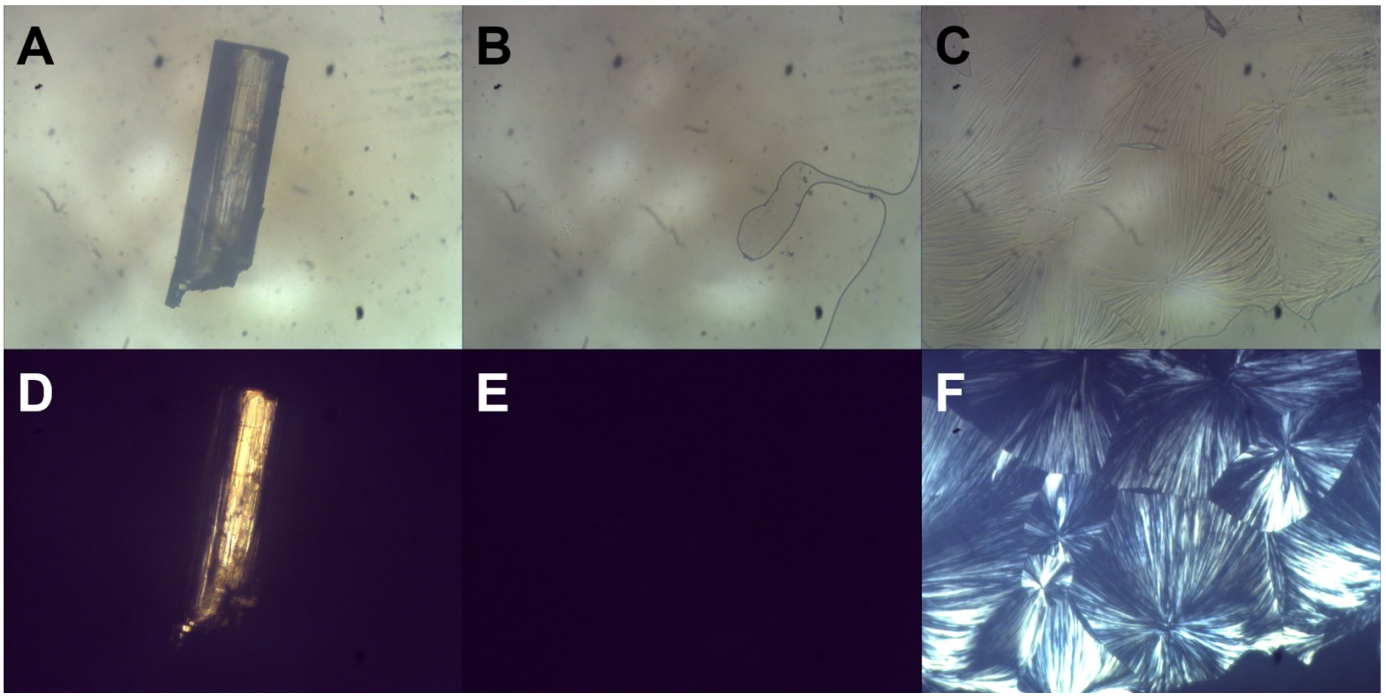

Figure 7. Thermomicroscopic analysis of TCZ-Ms crystals under white (A-C) and polarized (D-F) light. A and D) Before the melting point; B and E) After the melting point; C and F) After cooling the melted solid.

 ©AUTHOR(S)

Monitoring of the solid was also performed by MIR spectroscopy (Figure 8A). Linear regression analysis between spectra[18] in the wavenumber range 4000-400 cm^{-1} revealed that the solid exhibited some differences between the spectra of the first and remaining cycles (*r* 0.8768 and 0.8854, for cycles 1 vs. 4 and 1 vs. 8, respectively; *n* 1868), while essentially the same spectra were recorded for cycles other than the first (*r* 0.9905, for cycles 4 vs. 8; *n* 1868).

MIR spectroscopy is extremely sensitive to hydrogen bonding and its strength; even within the same crystallographic phase, heating can affect long-range H-bond order and reduce cooperative hydrogen bonding, increasing disorder; therefore, upon cooling, a slightly different H-bond arrangement may form, with the same space group, but different microstructure, not entailing polymorphism, but just reorganization. In line with previous observations, these also suggest that no decomposition takes place under the test conditions (≤ 230 °C).

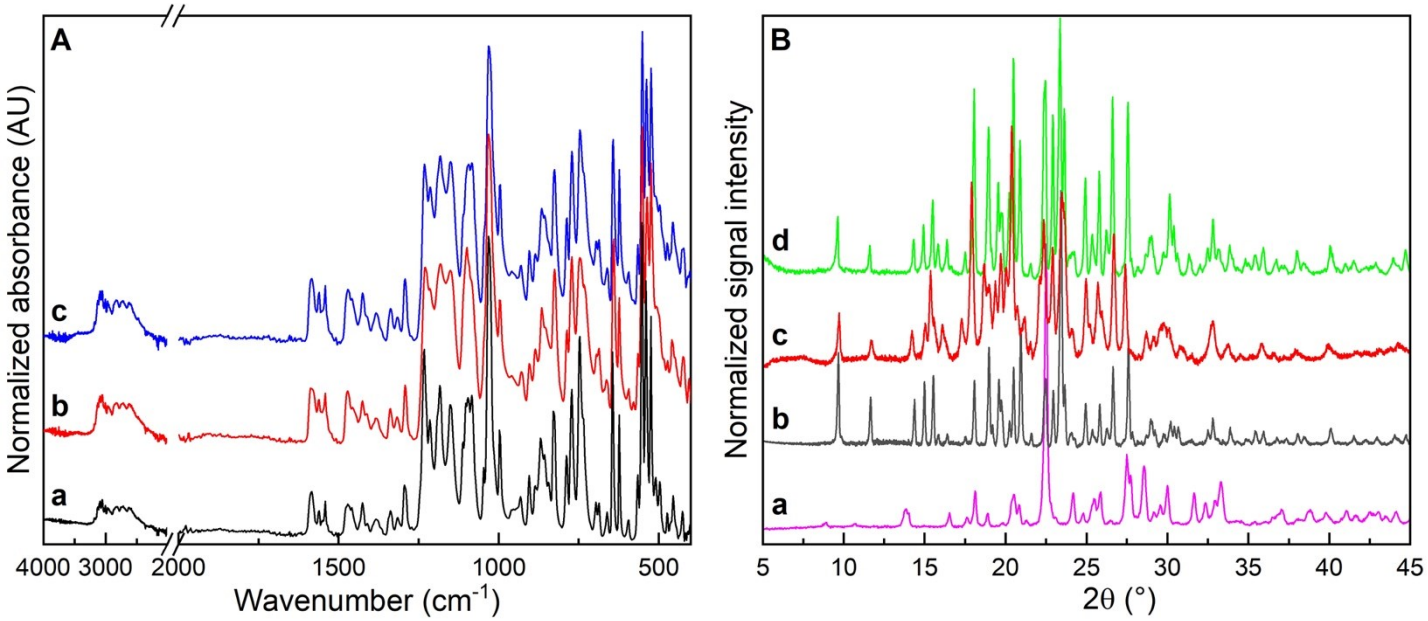

Figure 8. Thermal stability of TSC-Ms, as assessed by infrared (left) and PXRD (right) monitoring. A) Infrared spectroscopy; a) original spectrum; b) after 4 heating/cooling cycles; c) after 8 heating/cooling cycles. B) PXRD; a) TCZ; b) original curve of TCZ-Ms; c) after 4 heating/cooling cycles; d) curve of the solid phase aged for 14 months.

The results of the PXRD monitoring (Figure 8B) sustained this conjecture: despite some shape and intensity changes, no new peaks were observed in the curve of the fourth heating and cooling cycle with regards to the original trace (Figures 8Bc and 8Bb). In addition, considering that $MeSO_3H$ may have some degree of volatility (boiling point ~167 °C), it was confirmed that no traces of TCZ (Figure 8Ba) were present in the sample submitted to eight heating and cooling cycles.

Finally, it was also observed that the solid proved to be stable at room temperature for at least 14 months, since the curve of the originally prepared solid phase (Figure 8Bb) and that of the aged TCZ-Ms (Figure 8Bd) displayed the same set of peaks and no new peaks were observed in the aged sample.

 ©AUTHOR(S)

Conclusions

The widely used antifungal agent tioconazole is poorly soluble in water; however, the mesylate salt (TMZ-Ms) holds the promise of being a stable and non-hygroscopic alternative with improved solubility, which can eventually replace the base (TCZ) when solubility and/or bioavailability are critical issues.

New valuable data have been added to the analytical profile of the salt, including conditions for the preparation of single crystals and the results of its SCXRD structural elucidation along with the corresponding Hirshfeld surface analysis. In addition, an exhaustive and rational analysis of the ATR/MIR spectrum of the salt was made with the aid of theoretical calculations, which gave band frequency results in excellent agreement with the experimental observations.

Improved information on the thermal stability of TCZ-Ms have also been provided, verifying that despite the solid is stable beyond its melting point, repeated heating and cooling cycles are capable to induce small modifications in the solid phase, but no degradation. Finally, solution NMR analysis confirmed the phase is anhydrous, sustained the 1:1 stoichiometry of the salt and revealed the site of protonation.

All these new findings turn the analytical profile of TCZ-Ms into a more comprehensive body of knowledge on this solid, which may be useful at the time of designing new formulations based on this drug.

Experimental Section

API and chemicals and general:

Pharmaceutical grade TCZ bulk drug was kindly donated by Panalab Laboratories (Buenos Aires, Argentina). Analytical grade methanesulfonic acid, Et_2O and $CHCl_3$ were acquired from Merck Co. (Darmstadt, Germany). Double distilled water was used when required. The remaining solvents and reagents employed were of analytical grade.

Preparation of tioconazole mesylate (TCZ-Ms)

Methanesulfonic acid (MsOH, 0.10 mL, 1.55 mmol) was added to a solution of TCZ (600 mg, 1.55 mmol) in Et_2O (10 mL), and the resulting solution was stirred overnight at room temperature, when a suspension was formed. The solids were allowed to settle, affording a compact mass, which enabled the supernatant to be discarded. The solid residue (720 mg, 1.49 mmol, 96%) was dried at room temperature until constant weight. Single crystals suitable for SCXRD measurement were prepared by dissolving an aliquot of the bulk phase in $CHCl_3$ and allowing to stand the solution at room temperature in capped Khan tubes. The bulk batch of TCZ-Ms and the crystals of the salt were stored in a desiccator, protected from light.

Single-crystal X-ray diffraction

Crystallographic data for TCZ-Ms were obtained using a Bruker D8 QUEST ECO diffractometer (Bruker AXS GmbH, Karlsruhe, Germany) equipped with a PHOTON II CPAD area detector, using MoK radiation. For structure refinement, all H atoms were initially identified using a Fourier difference map. Hydrogens bonded to C were further idealized [C-H (sp^2) 0.93 Å; C-H_2 (sp^3) 0.97 Å; C-H_3 (sp^3) 0.96 Å] and refined using a riding model, while hydrogens bonded to a nitrogen atom were refined with restricted distances [N-H 0.86–0.89 Å]. Hydrogen atoms were treated isotropically with Uiso(H) 1.5 Ueq(X) for methyl and ammonium or 1.2 Ueq(X) for aromatics and others, and anisotropic shift parameters were used for atoms other than hydrogen.

Data from the elucidated crystal structures were deposited as a Crystallographic Information File (CIF) at the Cambridge Crystallographic Data Centre (CCDC). For the SCXRD experiments, the data collection and

 ©AUTHOR(S)

reduction strategy followed standard procedures implemented in the APEX4[19] software (Bruker, Billerica, MA, USA). The structure was solved with SHELXS-97[20] and refined using the full-matrix least squares procedure with SHELXL-2019/1.[21] Multiscan absorption correction was performed using SADABS 2016/2.[22] The crystallographic tables and figures were prepared using WinGX,[23] PLATON,[24] and Mercury.[25]

Hirshfeld surface

The three-dimensional Hirshfeld surface[26] of TCZ-Ms was visualized through a d_{norm} (normalized contact distance) graph and the two-dimensional fingerprint graphs[27] were generated with the Crystal Explorer v.17.5 software.[28]

Powder X-ray diffraction

The PXRD studies were performed at room temperature in a Bruker D2 Phaser diffractometer in the Bragg-Brentano configuration, employing Cu Kα radiation (1.54184 Å) from a 0.5 mm Ni-filtered source. The equipment was fitted with a primary divergence slit (1 mm) and an air scatter screen (2 mm), along with primary and secondary Soller slits (2.5°), and a SSD160-2 silicon strips detector, operating at 40 kV and a current of 10 mA. The samples were placed in a steel backloading sample holder and rotated at 15 rpm. The diffraction data were acquired over the 2θ range of 5–45°, at a scanning step of 0.026°, with a counting time of 1.5 s per step (42 min/sample).

Thermomicroscopy

The hot stage and optical microscopy determinations were performed with a Leitz model 350 microscope (Ernst Leitz GmbH, Wetzlar, Germany) equipped with a 10× eyepiece and a controllable heated stage. Solid samples were spread between two coverslips, and the system was placed in the heated stage, which was positioned below the microscope objective. The samples were observed under white and polarized light. Photographs were taken Biokan UCMOS 05100KPA USB 2.0 digital camera (Biokan Health Products Industry and Trade Co. Ltd., Kayseri, Turkey) at a 5.0 MP resolution [2592 × 1944 (H × V)].

Differential scanning calorimetry

The DSC curves were obtained with a Linseis PT1000 instrument (Linseis Messgeraete GmbH, Selb, Germany), where the samples (∼5 mg) were placed in open aluminum pans and an empty pan was employed as a reference. The samples were heated 10 °C min^{-1} in the range 40-230 °C, under an inert atmosphere provided by a constant flow of nitrogen (130 mL^{-1}).

Nuclear magnetic resonance spectroscopy

The NMR spectra were recorded on a Bruker Avance II 400 FT-NMR spectrometer (400.13 MHz for ^{1}H NMR and 100.62 MHz for ^{13}C NMR) in DMSO-d_6 (See Table 2 below). The chemical shifts are reported in ppm in the δ scale; the residual solvent peaks of DMSO (δ_H 2.49 ppm; δ_C 39.5 ppm) were used as internal references.

Mid-infrared spectroscopy

Mid-infrared (MIR) spectra were obtained with a GladiATR diamond-based attenuated total reflection (ATR) accessory coupled to a Shimadzu Prestige 21 FTIR spectrometer (Shimadzu Corp., Kyoto, Japan). The spectra were obtained on ∼20 mg samples along the 4000-400 cm^{-1} wavenumber range, acquiring 20 scans/spectrum at 4 cm^{-1} resolution.

Theoretical calculations

The assignments of the most important bands of TCZ-Ms were performed with the aid of theoretical calculations, carried out with the Gaussian-09 package.[29]

 ©AUTHOR(S)

Table 2. Assignment of the ^{1}H, ^{13}C and ^{15}N NMR spectroscopy data of TCZ-Ms dissolved in DMSO-d_6. Comparison of the ^{13}C and ^{15}N NMR chemical shifts with TCZ[a]

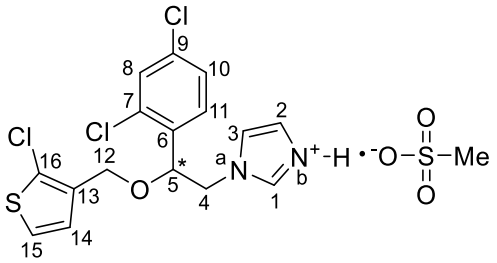

Position	TCZ-Ms					TCZ	Δδ
N°	^{1}H	^{13}C	COSY	HSQC	HMBC	^{13}C	(ppm)
1	9.04 (1H, bs)	136.1	H2, H3	+	C2, C3	137.7	-1.6
2	7.67 (1H, t, *J* = 1.6)	119.7	H1, H3	+	C1,	128.2	-8.5
3	7.62 (1H, t, *J* = 1.6)	122.7	H1, H2	+	C1,	119.9	2.8
4	4.47 (1H, dd, *J* = 7.5, 14.3)	51.8	H5	+	C1, C3, C5	50.0	1.8
	4.52 (1H, dd, *J* = 3.8, 14.3)						
5	5.09 (1H, dd, *J* = 3.8, 7.5)	75.0	H4	+	C4, C7, C11, C12	76.4	-1.4
6		134.0				134.7	-0.7
7		133.2				133.1	0.1
8	7.73 (1H, d, *J* = 2.2)	129.3	H10	+	C6, C7, C10	128.9	0.4
9		133.5				133.5	0
10	7.54 (dd, 1H, *J* = 2.2, 8.5)	128.0	H8, H11	+	C6, C8, C9	127.8	0.2
11	7.41 (1H, d, *J* = 8.5)	129.2	H10	+	C5,	129.3	-0.1
12	4.29 (1H, d, *J* = 12.2)	63.1		+	C5, C13, C14, C16	63.2	-0.1
	4.39 (1H, d, *J* = 12.2)						
13		126.8				126.3	0.5
14	6.89 (d, 1H, d, *J* = 5.7)	128.0	H15	+	C12, C13, C15, C16	127.9	0.1
15	7.42 (d, 1H, d, *J* = 5.7)	124.6	H14	+	C13, C14, C16	124.5	0.1
16		134.3				134.7	0.4
17 ($N^{+}H$)	4.03 (bs, 1H)	-					
$MeSO_3^{-}$	2.33 (s, 3H)	39.5		+			
N_a		-203.5[b]			H1, H2, H3, H4, H5	-212.0[b]	8.5
N_b		-203.5[b]			H1, H2	-118.7[b]	-84.8

[a]Chemical shifts (δ) are in ppm; coupling constants (*J*) are in Herz.
[b]Data are ^{15}N chemical shifts, taken from the corresponding ^{15}N HMBC spectra.

The input geometry of TCZ-Ms was taken from the corresponding crystal structure with normalized H-atom positions and fully optimized using the B3LYP density functional method with the basis set 6-311++G(d,p). Frequency calculations were carried out at the same computational level, and a scaling factor of 0.9613 was subsequently applied. All normal vibrational modes for the optimized structures have positive frequencies, indicating a local minimum on the potential energy hypersurface.

 ©AUTHOR(S)

Acknowledgements

The authors gratefully acknowledge Consejo Nacional de Investigaciones Científicas y Técnicas (CONICET, PIP 2021-0765), Agencia Santafesina de Ciencia, Tecnología e Innovación (ASACTEI, PEIC I+D-2023-004) and National University of Rosario (UNR, Project 80020230300051UR) for financial support. ABM and MFS thank CONICET for their postdoctoral and doctoral fellowships, respectively. The authors are grateful to the FAIRE program provided by the Cambridge Crystallographic Data Centre (CCDC) for the opportunity to use the Cambridge Structural Database (CSD) and associated software. The theoretical calculations have been performed at the facilities of the CCT-Rosario Computational Center, member of the High-Performance Computing National System (SNCAD, MincyT-Argentina).

Supplementary Material

Copies of 1D and 2D ^{1}H, ^{13}C, and ^{15}N NMR spectra. Tables containing NMR and MIR signal assignments, thermal stability details and critical crystallographic information.

References

1. Al-Alshaikh, M. A.; Mary, S.; Panicker, C. Y.; Ali, M. I. A.; El-Emam, A.; Alsenoy, C. V. *J. Mol. Struct.*, **2016**, *1109*, 131–138. https://doi.org/10.1016/j.molstruc.2015.12.075
2. Sanli, S.; Basaran, F.; Sanli, N.; Akmese, B.; Bulduk, I. *J. Sol. Chem.*, **2013**, *42*, 1976–1987. https://doi.org/10.1007/s10953-013-0083-x
3. Crisóstomo-Lucas, C.; García-Holley, P.; Hernández-Ortega, S.; Sánchez-Bartéz, F.; Gracía-Mora, I.; Barba-Behrens, N. *Inorg. Chim. Acta*, **2015**, *438*, 245–254. https://doi.org/10.1016/j.ica.2012.11.026
4. Brown, E. D.; El Zahed, S. S.; Farha, M. A.; French, S.; Kumar, G. *Antimicrob. Agents Chemother.*, **2021**, *65*, E01925–20. https://doi.org/10.1128/AAC.01925-20
5. Stratton, C. F.; Newman, D. J.; Tan, D. S. *Bioorg. Med. Chem. Lett*., **2015**, *25*, 4802–4807. https://doi.org/10.1016/j.bmcl.2015.07.014
6. Moroni, A. B.; Perez Mayoral, E.; Lionello, D. F.; Vega, D. R.; Kaufman, T. S.; Calvo, N. L. *Int. J. Pharm.*, **2023**, *637*, 122869. https://doi.org/10.1016/j.ijpharm.2023.122869
7. Drozd, K. V.; Manin, A. N.; Boycov, D. E.; Churakov, A. V.; Perlovich, G. L. *Cryst. Growth Des*., **2021**, *21*, 7285−7297. https://doi.org/10.1021/acs.cgd.1c01139
8. Zhang, W.; Ramamoorthy. Y.; Kilicarslan, T.; Nolte, H.; Tyndale, R. F.; Sellers, E. M. *Drug Metab. Dispos.*, **2002**; *30*, 314–318. https://doi.org/10.1124/dmd.30.3.314
9. Kljun, J.; Scott, A. J.; Lanišnik Rižner, T.; Keiser, J.; Turel, I. *Organometallics*, **2014**, *33*, 1594−1601. https://doi.org/10.1021/om401096y

 ©AUTHOR(S)

10. Madhesiya, A.; Dash, S. G.; Gupta, P.; Akhir, A.; Saxena, D.; Maitra, R.; Chopra, S.; Thakur, T. S. *CrystEngComm*, **2023**, *25*, 6758−6776. https://doi.org/10.1039/D3CE00948C
11. Moroni, A. B.; Pérez Mayoral, E.; Lionello, D. F.; Vega, D. R.; Kaufman, T. S.; Calvo, N. L. *Int. J. Pharm.*, **2024**, *652*, 123855. https://doi.org/10.1016/j.ijpharm.2024.123855
12. Moroni, A. B.; Bottoso, T.; Lionello, D. F.; Vega, D. R.; Kaufman, T. S.; Calvo, N. L. *Acta Cryst. E*, **2024**, *80*, 1064–1068. https://doi.org/10.1107/S2056989024009204
13. Moroni, A. B.; Bottoso, T.; Lionello, D. F.; Vega, D. R.; Kaufman, T. S.; Calvo, N. L. *Cryst. Growth. Des.*, **2025**, *25*, 2172–2185. https://doi.org/10.1021/acs.cgd.5c00130
14. Yu, L. X.; Carlin, A. S.; Amidon, G. L.; Hussain, A. S. *Int. J. Pharm.*, **2024**, *270*, 221–227. https://doi.org/10.1016/j.ijpharm.2003.10.016
15. Bharate, S. S. *J. Drug Deliv. Sci. Technol.*, **2021**, *66*, 102913. https://doi.org/10.1016/j.jddst.2021.102913
16. Seth, S. K.; Saha, N. C.; Ghosh, S.; Kar, T. *Chem. Phys. Lett.*, **2011**, *506*, 309–314. https://doi.org/10.1016/j.cplett.2011.03.033
17. Reena Kumar, A., Singh, P., Deval, V., Gupta, A. *Polycycl. Aromat. Comp.*, **2024**, *44*, 1644–1668. https://doi.org/10.1080/10406638.2023.2201461n
18. Moroni, A. B.; Pérez Mayoral, E.; Lionello, D. F.; Vega, D. R.; Kaufman, T. S.; Calvo, N. L. *Eur. J. Pharm. Biopharm.*, **2023**, *184*, 25–35. https://doi.org/10.1016/j.ejpb.2023.01.008
19. Bruker (2019). APEX4 and SAINT. Bruker AXS Inc.; Madison, Wisconsin, USA.
20. Sheldrick, G. M. *Acta Cryst.*, **2008**, *A64*, 112–122. https://doi.org/10.1107/S0108767307043930
21. Sheldrick, G. M. *Acta Cryst*., **2015**, *C71*, 3–8. https://doi.org/10.1107/S2053229614024218
22. Krause, L.; Herbst-Irmer, R.; Sheldrick, G. M.; Stalke, D. *J. Appl. Crystallogr.*, **2015**, *48*, 3–10. https://doi.org/10.1107/S1600576714022985
23. Farrugia, L. J. *J. Appl. Cryst*., **2012**, *45*, 849–854. https://doi.org/10.1107/S0021889812029111
24. Spek, A. L. *Acta Cryst.*, **2009**, *D65*, 148–155. https://doi.org/10.1107/S090744490804362X
25. Macrae, C. F.; Bruno, I. J.; Chisholm, J. A.; Edgington, P. R.; McCabe, P.; Pidcock, E.; Rodriguez-Monge, L.; Taylor, R.; van de Streek, J.; Wood, P. A. *J. Appl. Cryst.*, **2008**, *41*, 466–470. https://doi.org/10.1107/S0021889807067908
26. McKinnon, J. J.; Jayatilaka, D.; Spackman, M. A. *Chem. Commun*., **2007**, 3814–3816. https://doi.org/10.1039/B704980C
27. Spackman, M. A.; McKinnon, J. J. *CrystEngComm*, **2002**, *4*, 378–392. https://doi.org/10.1039/B203191B
28. packman, P. R.; Turner, M. J.; McKinnon, J. J.; Wolff, S. K.; Grimwood, D. J.; Jayatilaka, D.; Spackman, M. A. *J. Appl. Cryst.*, **2021**, *54*, 1006–1011. https://doi.org/10.1107/S1600576721002910

 ©AUTHOR(S)

29. Frisch, M. J.; Trucks, G. W.; Schlegel, H. B.; Scuseria, G. E.; Robb, M. A.; Cheeseman, J. R.; Scalmani, G.; Barone, V.; Mennucci, B.; Petersson, G. A.; Nakatsuji, H.; Caricato, M.; Li, X.; Hratchian, H. P.; Izmaylov, A. F.; Bloino, J.; Zheng, G.; Sonnenberg, J. L.; Hada, M.; Ehara, M.; Toyota, K.; Fukuda, R.; Hasegawa, J.; Ishida, M.; Nakajima, T.; Honda, Y.; Kitao, O.; Nakai, H.; Vreven, T.; Montgomery, J. A., Jr.; Peralta, J. E.; Ogliaro, F.; Bearpark, M.; Heyd, J. J.; Brothers, E.; Kudin, K. N.; Staroverov, V. N.; Kobayashi, R.; Normand, J.; Raghavachari, K.; Rendell, A.; Burant, J. C.; Iyengar, S. S.; Tomasi, J.; Cossi, M.; Rega, N.; Millam, J. M.; Klene, M.; Knox, J. E.; Cross, J. B.; Bakken, V.; Adamo, C.; Jaramillo, J.; Gomperts, R.; Stratmann, R. E.; Yazyev, O.; Austin, A. J.; Cammi, R.; Pomelli, C.; Ochterski, J. W.; Martin, R. L.; Morokuma, K.; Zakrzewski, V. G.; Voth, G. A.; Salvador, P.; Dannenberg, J. J.; Dapprich, S.; Daniels, A. D.; Farkas, O.; Foresman, J. B.; Ortiz, J. V.; Cioslowski, J.; Fox, D. J. Gaussian 09, Revision D.01; Gaussian, Inc.: Wallingford, CT, 2009.

This paper is an open access article distributed under the terms of the Creative Commons Attribution (CC BY) license (http://creativecommons.org/licenses/by/4.0/)

 ©AUTHOR(S)